



CHALMERS
UNIVERSITY OF TECHNOLOGY

Direct measurement of key exciton properties: Energy, dynamics, and spatial distribution of the wave function

Downloaded from: <https://research.chalmers.se>, 2024-11-19 05:18 UTC













Citation for the original published paper (version of record):

Dong, S., Puppin, M., Pincelli, T. et al (2021). Direct measurement of key exciton properties: Energy, dynamics, and spatial distribution of the wave function. *Natural Sciences*, 1(1). <http://dx.doi.org/10.1002/ntls.10010>

N.B. When citing this work, cite the original published paper.

RESEARCH ARTICLE

Direct measurement of key exciton properties: Energy, dynamics, and spatial distribution of the wave function

Shuo Dong¹  | Michele Puppini^{1,2}  | Tommaso Pincelli¹  | Samuel Beaulieu¹  |
 Dominik Christiansen³ | Hannes Hübener⁴  | Christopher W. Nicholson^{1,5}  |
 Rui Patrick Xian¹  | Maciej Dendzik^{1,6}  | Yunpei Deng^{1,7} |
 Yoav William Windsor¹  | Malte Selig³ | Ermin Malic⁸ | Angel Rubio⁴  |
 Andreas Knorr³ | Martin Wolf¹ | Laurenz Rettig¹  | Ralph Ernstorfer¹ 

¹ Fritz-Haber-Institut der Max-Planck-Gesellschaft, Berlin, Germany

² Laboratoire de Spectroscopie Ultrarapide and Lausanne Centre for Ultrafast Science (LACUS), École polytechnique fédérale de Lausanne, ISIC, Lausanne, Switzerland

³ Institut für Theoretische Physik, Nichtlineare Optik und Quantenelektronik, Technische Universität Berlin, Berlin, Germany

⁴ Max Planck Institute for the Structure and Dynamics of Matter and Center for Free Electron Laser Science, Hamburg, Germany

⁵ Département de Physique and Fribourg Center for Nanomaterials, Université de Fribourg, Fribourg, Switzerland

⁶ Department of Applied Physics, KTH Royal Institute of Technology, Stockholm, Sweden

⁷ SwissFEL, Paul Scherrer Institute, Villigen, Switzerland

⁸ Department of Physics, Chalmers University of Technology, Gothenburg, Sweden

Correspondence

Shuo Dong, Laurenz Rettig, and Ralph Ernstorfer, Fritz-Haber-Institut der Max-Planck-Gesellschaft, Faradayweg 4–6, Berlin 14195, Germany.

Email: dong@fhi-berlin.mpg.de, rettig@fhi-berlin.mpg.de, and ernstorfer@fhi-berlin.mpg.de

Shuo Dong and Michele Puppini contributed equally to this work.

This Research Paper is showcased in a Highlight entitled *Disclosed: Quasiparticle properties and dynamics in real and momentum space* <https://doi.org/10.1002/ntls.10017>.

Funding information

Canadian Network for Research and Innovation in Machining Technology, Natural Sciences and Engineering Research Council of Canada; Alexander von Humboldt-Stiftung; European Commission, Grant/Award Number: 899794; H2020 European Research Council, Grant/Award Numbers: ERC-2015-AdG-694097, RC-2015-CoG-682843; Max-Planck-Gesellschaft; Deutsche Forschungsgemeinschaft, Grant/Award Numbers: 182087777, B12, B17, FOR1700, project E5, SPP2244, 443366970, RE 3977/1, SFB/TRR227, A09, B07

Abstract: Excitons, Coulomb-bound electron–hole pairs, are the fundamental excitations governing the optoelectronic properties of semiconductors. Although optical signatures of excitons have been studied extensively, experimental access to the excitonic wave function itself has been elusive. Using multidimensional photoemission spectroscopy, we present a momentum-, energy-, and time-resolved perspective on excitons in the layered semiconductor WSe_2 . By tuning the excitation wavelength, we determine the energy–momentum signature of bright exciton formation and its difference from conventional single-particle excited states. The multidimensional data allow to retrieve fundamental exciton properties like the binding energy and the exciton–lattice coupling and to reconstruct the real-space excitonic distribution function via Fourier transform. All quantities are in excellent agreement with microscopic calculations. Our approach provides a full characterization of the exciton properties and is applicable to bright and dark excitons in semiconducting materials, heterostructures, and devices.

Key points:

- The full life cycle of excitons is recorded with time- and angle-resolved photoemission spectroscopy.
- The real-space distribution of the excitonic wave function is visualized.
- Direct measurement of the exciton-phonon interaction.

KEYWORDS

condensed matter physics, exciton physics, many-body physics, quasi-particle interactions, semiconductors, time-resolved photoemission spectroscopy, ultrafast dynamics

This is an open access article under the terms of the [Creative Commons Attribution](https://creativecommons.org/licenses/by/4.0/) License, which permits use, distribution and reproduction in any medium, provided the original work is properly cited.

© 2021 The Authors. *Natural Sciences* published by Wiley-VCH GmbH

Excitons, bound electron–hole quasi-particles carrying energy and momentum but no net charge, are fundamental excitations of semiconductors and insulators arising from light–matter interaction [1]. An initial excitonic polarization induced by a light field (often referred to as coherent excitons and, e.g., detected by optical absorption spectroscopy) rapidly loses coherence with the driving field and dephases into a population of incoherent excitonic states [2, 3]. The generated excitons propagate in solid-state materials through diffusion [4, 5] and eventually release their energy, for example, in the form of luminescence (photon), lattice excitation (phonon), or dissociation into single-charged quasi-particles [6–9]. Understanding exciton physics is of capital importance for advanced photonic and optoelectronic applications including photovoltaics. Layered transition metal dichalcogenide (TMDC) semiconductors exhibit rich exciton physics even at room temperature due to strong Coulomb interaction [10]. Excitons in TMDCs feature large oscillator strength [11] and their inter- and intraband dynamics have been extensively investigated [12–14]. Moreover, strong spin–orbit coupling and broken inversion symmetry in each crystalline trilayer lead to a locking between spin, valley, and layer degrees of freedom, which started a surge of valley physics studies [15–17].

A large portion of the research on excitonic phenomena in TMDCs adopts optical spectroscopic techniques [10, 12, 14–16, 18–21], which only access bright excitonic transitions with near-zero momentum transfer. Although techniques such as time-resolved THz spectroscopy also allow probing optically dark excitons via internal quantum transitions [13], finite-momentum excitons that lie outside the radiative light cone remain inaccessible to such methods. This limitation is overcome by time- and angle-resolved photoemission spectroscopy (trARPES), a spectroscopic tool accessing excited states, including excitons, in energy–momentum space and on ultrafast time scales [17, 22–24]. Here, we reveal the characteristics of the excitonic wave function in the photoemission signal of the prototypical layered TMDC semiconductor 2H-WSe₂ and establish that all fundamental exciton properties are encoded in the trARPES signal's energy, time, and momentum dimensions: the exciton binding energy, its self-energy as measure of the exciton–lattice coupling, as well as the real-space distribution of the excitonic wave function.

Figure 1a depicts the experimental scheme of trARPES employing femtosecond near-infrared pump and extreme ultraviolet (XUV) probe pulses combined with two types of photoelectron analyzers: a hemispherical analyzer (HA) and a time-of-flight momentum microscope (MM). The whole setup allows us to measure the three-dimensional (3D) time-dependent electronic structure in a given energy–momentum-plane with high counting statistics using the HA, and alternatively resolve both in-plane momentum directions yielding a four-dimensional (4D) photoemission signal $I(E_{kin}, k_x, k_y, t)$ of the entire valence band with the MM [21, 25]. Figure 1b–d and e–g show snapshots of the 3D and 4D data with 1.55 eV excitation, respectively, at three selected time delays: (i) prior to optical excitation, showing the ground-state band structure of WSe₂ from the Brillouin zone (BZ) center Γ (only shown in the MM data) to the BZ boundary K

points (b and e); (ii) upon optical excitation resonant with the A exciton absorption (the first excitonic state), featuring excited-state signal at the K and Σ valleys (c and f); and (iii) at $t = 100$ fs after optical excitation, with excited-state signal mostly at the Σ valleys (d and g). In the following, we identify the excitonic features in the excited state photoemission signal and quantify the exciton properties retrieved from the energy, time, and momentum dimensions of the 4D trARPES signal.

PHOTOEMISSION SIGNATURE OF EXCITONS

During the photoemission of an electron bound in an exciton, the electron–hole interaction diminishes, that is, the exciton breaks up, as a single-particle photoelectron is detected while a single-particle hole is left behind in the material [23]. To identify the signature of the excitonic electron–hole interaction in photoemission spectroscopy, we compare the signal of excitons with that of single-particle excited states. For generating excitons, we excite with 1.55 eV photons ($1/e^2$ bandwidth = 43 meV), in resonance with the low-energy side of the A-excitonic absorption of bulk WSe₂ [12]. Figure 2a shows the excited-state signal integrated in the first 25 fs after pump–probe overlap. The data reveal a vertical transition at the K point through an excited-state signal localized in energy and momentum. In contrast, the above-band-gap excitation with 3.1 eV photon energy generates a population higher in the conduction band, which rapidly redistributes to all bands and valleys of the lower conduction band (the equivalent scenario applies to the holes in the valence band). Figure 2b shows this excited state signal in the K valley 100 fs after excitation, where carriers have redistributed in energy and momentum. This signal resembles the dispersion of a single-particle band with an effective mass of $m^* = 0.55 m_e$, in good agreement with electronic band structure calculations [26]. The energetic positions of the excitonic and single-particle states at the K point are determined as the center of mass of the energy distribution curves (EDCs), see Figure 2b. The excited-state signal upon resonant excitation of the A exciton is centered 100 ± 3 meV below the center of the single-particle band. Such a signal below the single-particle band has been predicted as photoemission signature of excitons and the energy difference can be associated with the exciton binding energy E_b [2, 3, 9, 27]. A calculation of the A-exciton binding energy in bilayer WSe₂ based on the screened Keldysh-like potential (see the Supporting Information for details) yields $E_b = 91.3$ meV, in very good agreement with the experimental value. It is important to note that we retrieve the exciton binding energy directly from measuring the absolute energies of many-body and single-particle states with a single photoemission experiment, in contrast to combining different experimental methods [18] or by comparing photoemission signals with electronic structure calculations [24]. The observation that the excitonic binding energy is measurable as energy loss of the photoelectron confirms that the hole final states indeed are identical to single-particle holes, which further implies that the localized hole of the exciton transforms to Bloch-like single-particle states during the photoemission process.

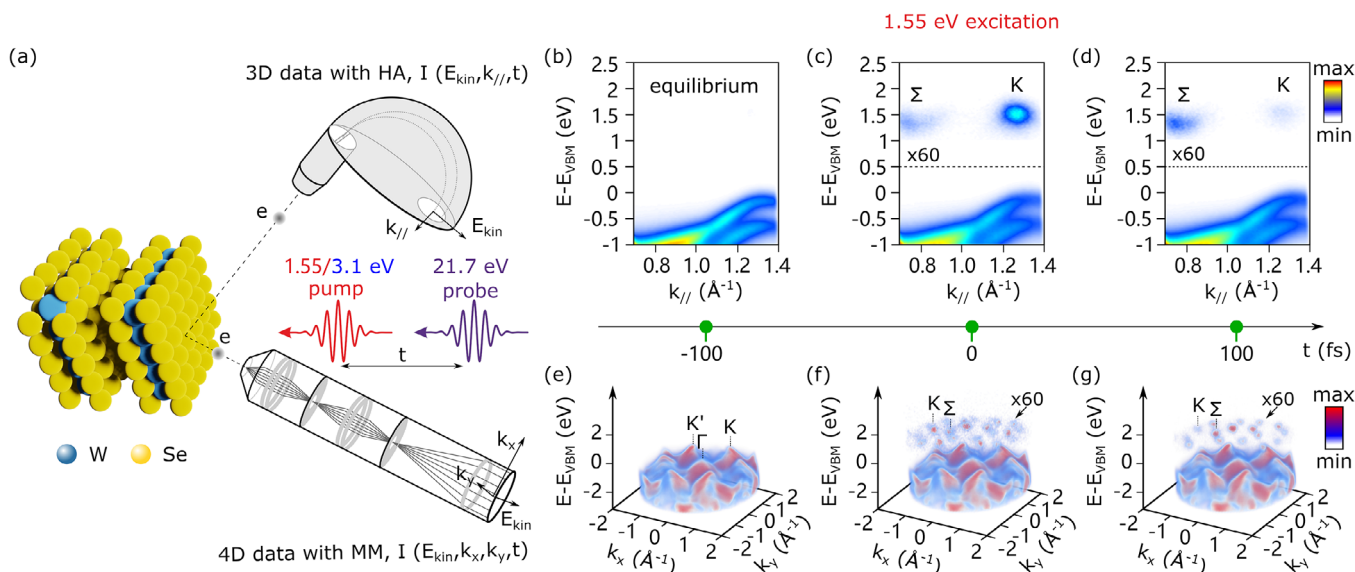


FIGURE 1 Multidimensional photoemission spectroscopy of excitons in WSe_2 : (a) Using near-infrared (1.55 eV) or UV (3.1 eV) pump and XUV probe (21.7 eV), we performed trARPES measurements in bulk WSe_2 with two types of photoelectron detectors: hemispherical analyzer (HA) or time-of-flight momentum microscope (MM). (b) With the HA, the equilibrium band structure in a finite momentum window is found at negative pump-probe delay, $t = -100$ fs, showing the spin-orbit split valence bands near the K-points. Upon 1.55 eV excitation, the excited state dynamics, that is, the intervalley scattering from K to Σ valley, are representatively shown in (c) $t = 0$ fs and (d) $t = 100$ fs. (e) Four-dimensional (4D) band structure mapping, $I(E, k_x, k_y, t)$, with the MM showing the band dispersion within the whole Brillouin zone from its center Γ to the K valleys at its corners. The same evolution of the excited state is shown for (f) $t = 0$ fs and (g) $t = 100$ fs, respectively. All the excited states signal are scaled for clarity

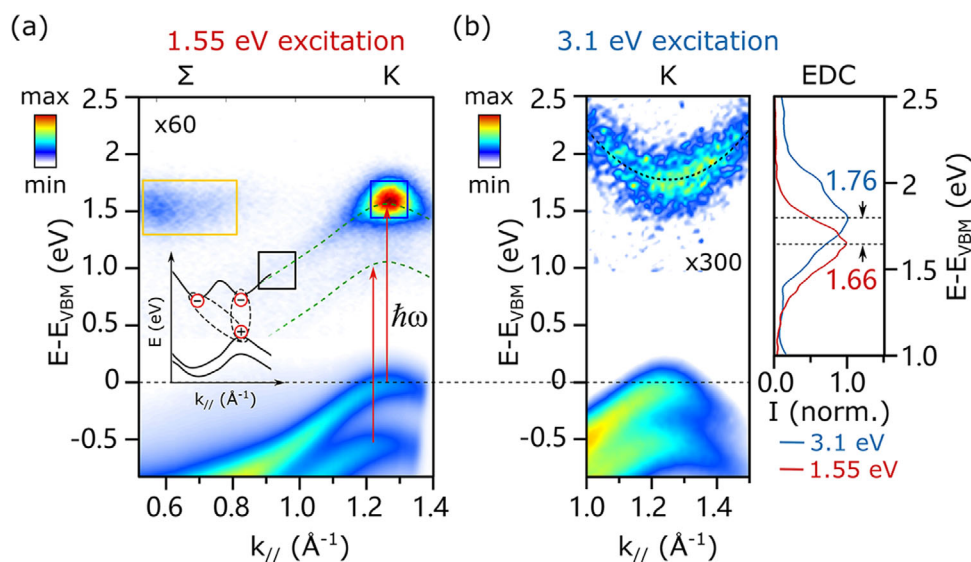


FIGURE 2 Signatures of excitons versus quasi-free carriers in trARPES. (a) Upon the arrival of the pump photons at $\hbar\omega = 1.55$ eV, the excited states at K and Σ are populated. During the pump-probe overlap, sideband replica of the two topmost valence bands, VB1 and VB2, are visible (highlighted by the green dashed lines). Inset: schematic of the bright exciton at the K valley and dark exciton at the Σ valley. (b) Using the above-band-gap pump at 3.1 eV, the parabolic dispersion of the conduction band at the K valley is clearly observed. As shown in the energy distribution curves (EDCs) at K (right panel), the single-particle (3.1 eV pump photon energy; blue) is $\Delta E \approx 100$ meV higher than the excitonic signal at 1.66 eV (1.55 eV pump photon energy; red). The excited state signals are scaled for clarity

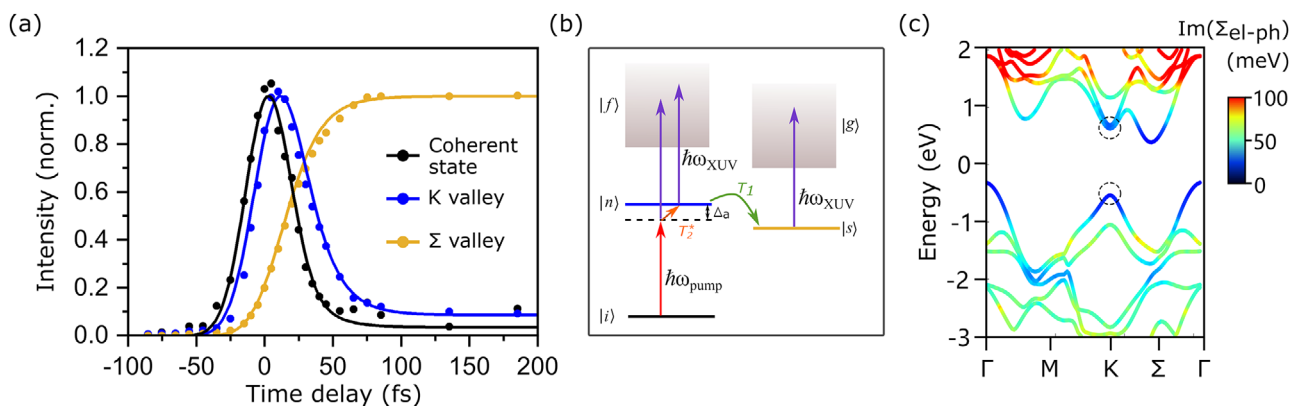


FIGURE 3 Exciton dephasing and population dynamics with optical Bloch equation (OBE) model fitting. (a) Normalized photoemission intensity of photon-dressed coherent state (black), bright exciton population at K (blue) and dark exciton at Σ (yellow) extracted from the three labeled regions of interest (ROIs) in Figure 2a, respectively. The observed time traces are fitted globally with the solution of OBEs (lines). (b) Schematic of the five-level OBE model: the initial state $|i\rangle$ is coherently coupled to the final state $|f\rangle$ through a virtual intermediate state (dashed line), which dephase to the bright excitons at state $|n\rangle$ with the time scale of T_2^* ; the population at state $|n\rangle$ scatters to the dark state $|s\rangle$ with the time scale of T_1 ; all the excited states are photoionized to the final states $|f\rangle$ and $|g\rangle$, respectively. (c) Imaginary part of the electron-phonon self-energy calculated using density functional perturbation theory. The values at the band extrema at K (circles) are compared with those estimated from the experimental exciton lifetime

To set the stage for discussing the exciton dynamics, we emphasize a signal appearing as replicas of the upper (VB1) and lower (VB2) spin-orbit split valence bands in Figure 2a shifted by the photon energy $\hbar\omega_{\text{pump}}$. This signal only appears during temporal pump-probe overlap and we attribute it to a photon-dressed electronic state due to coherent coupling to the optical driving field. As the employed s-polarized pump light (polarization parallel to the sample surface) suppresses laser-assisted photoemission, the experimental configuration selectively probes the coherent excitonic polarization induced by the pump field [2, 3, 28].

FORMATION AND DECAY DYNAMICS OF BRIGHT EXCITONS

The bright A excitons at the K point are not the lowest energy excitons in WSe₂ but can relax their energy further by scattering in momentum space. We extract the quasi-particle dynamics within three regions of interest (ROIs) from the trARPES data in Figure 2a, representing the coherent excitonic replica of VB1, the excitonic state at the K valley, and the Σ valley population. The respective time traces in Figure 3a reflect three types of quasi-particle dynamics: the dephasing of the coherent excitonic polarization (black), the buildup and relaxation of a bright exciton population at K (blue), and the carrier accumulation of dark states at Σ (yellow).

The observed carrier dynamics imply the following microscopic processes as sketched in Figure 3b. First, the interaction of the initial valence band state $|i\rangle$ with the near-resonant optical light field creates a coherent excitonic polarization (dashed line), which quickly dephases into an optically bright exciton population $|n\rangle$, offset by the pump detuning Δ_a . The decoherence process occurs with the pure dephasing

time T_2^* . These bright excitons undergo rapid scattering into the optically dark Σ -point state $|s\rangle$ on the time scale T_1 . We model these processes and the photoemission signals from these states into the continuum final states $|f\rangle$ and $|g\rangle$ using a five-level extension to the optical Bloch equations (OBEs; see the Supporting Information) [29, 30]. Based on a multivariate least-squares fitting procedure, we are able to describe the dynamics of coherent and incoherent exciton contributions, obtaining a coherent exciton dephasing time of $T_2^* = 17 \pm 9$ fs and a population lifetime for the bright A-exciton population of $T_1 = 18 \pm 4$ fs. The extracted dephasing time corresponds well to microscopic calculations [14, 31].

To evaluate the mechanism governing the bright exciton scattering, we performed *ab initio* calculations of the single-particle self-energy of WSe₂. At low excitation densities, the electron self-energy is dominated by electron-phonon interaction that is computed using density functional perturbation theory, taking into account the electronic screening of the lattice motion (see the Supporting Information). The imaginary part of the momentum-resolved self-energy is shown in Figure 3c encoded by the color scale. From the calculation, we obtain $\text{Im}(\Sigma_{\text{el-ph}}) = 13.1$ meV at the conduction band minimum and $\text{Im}(\Sigma_{\text{h-ph}}) = 2.6$ meV at the valence band maximum of the K valleys. Although a rigorous description of exciton-phonon coupling requires treatment on the basis of excitonic eigenstates, in the weak coupling limit, that is, small self-energy renormalization due to the electron-hole interaction, the exciton-phonon self-energy is dominated by its *incoherent* contribution [32]. In this case, the exciton-phonon interaction can be approximated as sum of the single-particle-phonon interactions. Our calculated value $\text{Im}(\Sigma_{\text{el-ph}}) + \text{Im}(\Sigma_{\text{h-ph}}) = 16$ meV agrees with the experimental exciton self-energy $\text{Im}(\Sigma_{\text{ex}}) = 18 \pm 4.8$ meV determined according to $\text{Im}(\Sigma_{\text{ex}}) = \hbar/(2T_1)$. This agreement with theory shows that the exciton lifetime provides a

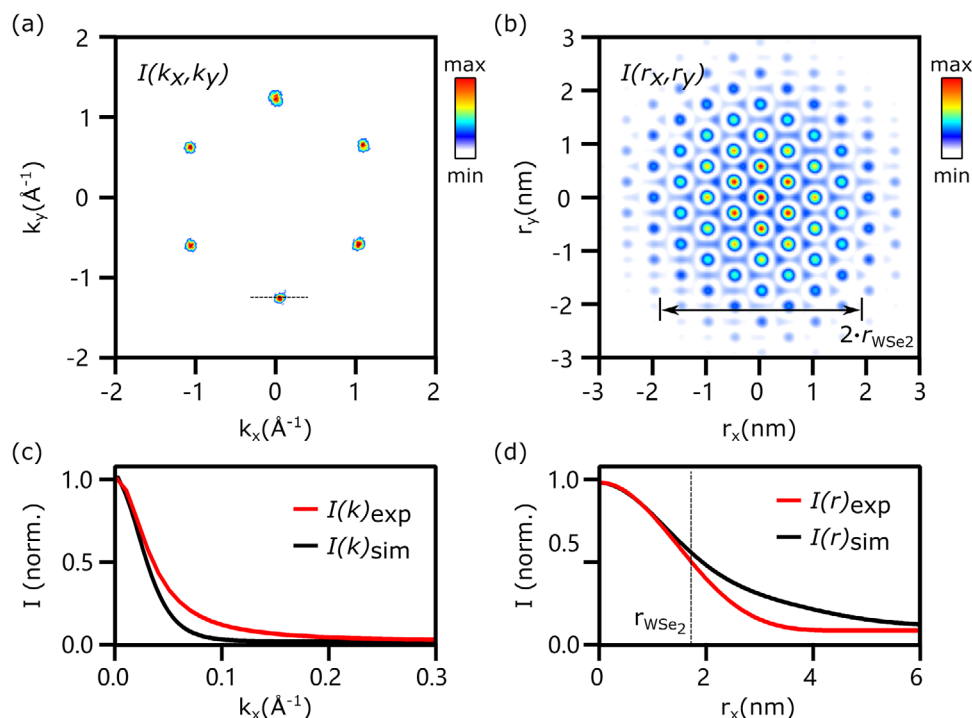


FIGURE 4 Momentum- and real-space distribution of A excitons in WSe₂. (a) The early-time momentum distribution of the exciton signal in the six K valleys, $I(k_x, k_y, t = 0 \text{ fs})$, obtained by energy integration over the conduction band. (b) Two-dimensional Fourier transform of the momentum-resolved photoemission intensity $I(k_x, k_y)$ recovers the real-space image $I(r_x, r_y)$, featuring the electron density distribution of the excitonic wave function. The high-frequency oscillations reflect the hexagonal lattice structure. The width of the exciton distribution is indicated by $2 \cdot r_{\text{WSe}_2}$. (c) The momentum distribution curve (MDC) of the bottom K valley (red) extracted along the dashed line in (a), compared with the calculated MDC of the A exciton (black). (d) Experimental and theoretical radial real-space exciton distribution. The exciton Bohr radius r_{WSe_2} is indicated with a dashed line. To retrieve the spatial distribution of the exciton, the oscillatory pattern in (b) is removed by Fourier-transforming only one of the K valleys (see the Supporting Information for details)

quantitative measure of the strength of its interaction with the lattice and supports the assumption of a dominating incoherent self-energy contribution.

MOMENTUM- AND REAL-SPACE DISTRIBUTION OF A EXCITONS

Our 4D trARPES data not only provide the energy-momentum dynamics of excitons, but also contain direct amplitude information about exciton wave functions. In Figure 4a, we display the early-time excited-state momentum distribution $I(k_x, k_y, t = 0 \text{ fs})$ of the K valleys, by integrating in energy over the conduction band. Signals from other valleys are filtered out in order to focus on the A excitons (see the Supporting Information). The total photoemission intensity is proportional to the squared transition dipole matrix element, $|M_{fi}^k|^2 = |\langle \psi_f | \mathbf{A} \cdot \mathbf{p} | \psi_i \rangle|^2$, which connects the initial state wave function ψ_i to the photoemission final state ψ_f , via the polarization operator $\mathbf{A} \cdot \mathbf{p}$. Here, \mathbf{A} is the vector potential of the light field and \mathbf{p} is the momentum operator. Within the plane wave approximation (PWA) for the final state, the matrix element takes the following form:

$$|M_{fi}^k|^2 \propto |\mathbf{A} \cdot \mathbf{k}|^2 |\langle e^{i\mathbf{k} \cdot \mathbf{r}} | \psi_i \rangle|^2, \quad (1)$$

where \mathbf{k} is the wave vector of the photoionized electron. According to Equation (1), the matrix element is proportional to the amplitude of the Fourier transform (FT) of the initial state wave function. Therefore, the momentum distribution of the photoemission signal $I(k_x, k_y)$ can be used to retrieve the real-space probability density of the electron contribution to the two-particle excitonic wave function, that is, the modulus-squared wave function $I(r_x, r_y)$, with a suitable assumption for the missing phase information.

A similar reconstruction of electronic wave functions from ARPES spectra has been previously demonstrated for occupied molecular orbitals in the ground state of crystalline organic films and chemisorbed molecular monolayers [33, 34]. Here, we extend this technique into the time domain and apply it to reconstruct the excitonic wave function in WSe₂. Assuming a constant phase profile across the BZ as a lower-limit wave function extension (see the Supporting Information), we retrieve the exciton probability density via two-dimensional FT as shown in Figure 4a and b. The reconstruction exhibits a broad isotropic real-space exciton distribution carrying high-frequency oscillations, corresponding to the hexagonal periodic lattice structure of WSe₂. To resolve the isotropic exciton wave function envelope more clearly, the one-dimensional real-space carrier distribution without the oscillatory pattern is shown in Figure 4d, obtained by FT of only one of the six K

valleys, yielding a value of $r_{\text{WSe}_2}^{\text{exp}} = 1.74 \pm 0.2$ nm for the excitonic Bohr radius.

To verify the method of reconstructing excitonic wave functions, we performed microscopic calculations of trARPES spectra. The momentum-resolved description of the exciton is based on a many-particle treatment of the Coulomb interaction between electron-hole pairs and the exciton-phonon scattering dynamics [3] (see the Supporting Information). The momentum distributions of the bright K excitons calculated within the PWA for the final state is shown in Figure 4c. We find very good agreement to the experimental momentum distribution curve (MDC) taken along the dashed line in Figure 4a, supporting our assumption that the trARPES spectrum contains the fingerprints of the excitonic wave function and justifying the use of the PWA. Furthermore, the calculated real-space exciton distribution in Figure 4d shows good agreement to our experimental results, yielding a very similar excitonic Bohr radius of $r_{\text{WSe}_2}^{\text{theo}} = 1.78$ nm. This agreement demonstrates the consistency of the experimentally retrieved exciton binding energy and Bohr radius and additionally suggests the validity of the assumption of a constant phase, which provides the FT-limited (lower bound) exciton distribution. Although the excitonic Bloch state is invariant under global and valley-dependent phase renormalization, we find that valley-local phase variations in momentum space can lead to broadening of the exciton probability distribution. In the Supporting Information, we reconstruct the real-space exciton density distribution with nonconstant intervalley and intravalley phase profiles, where we find a broadened exciton distribution in the case of an intravalley varying phase. Therefore, we note here that the real-space reconstruction of the exciton density with a constant phase is suitable for topologically trivial solid-state wave functions. However, the winding of the phase in topologically nontrivial materials leads to an additional expansion of the carrier density distribution, requiring explicit momentum-dependent phase information. In general, the phase of the excitonic wave function might additionally be reconstructed through iterative phase retrieval algorithms [35]. We envision that future developments will allow retrieving the phase as well as orbital information of excitonic wave functions by utilizing dichroic observables [36–38] in trARPES.

In this work, we provide a comprehensive experimental characterization of an excitonic state with trARPES. The interactions governing the formation of this prototypical many-body state are observable as energy renormalization in comparison to single-particle states, while its interaction strength with other quasi-particles is reflected in the excited state's lifetime. These quantities are intimately connected to the real and imaginary parts of the many-body state's self-energy and our approach establishes experimental access to these elusive quantities. Moreover, we retrieve real-space information of the excitons by FT of its momentum distribution, establishing the measurement of wave function properties of transient many-body states with 4D photoemission spectroscopy. Our approach is applicable to all exciton species occurring in a wide range of inorganic and organic semiconductors, van der Waals heterostructures, and devices. Its extension to other many-body quasi-particles in solids appears straightforward.

NOTE ADDED IN PROOF

Recently, Man et al. applied a similar approach for retrieving real-space information of excitons with time- and angle-resolved photoemission spectroscopy. Man MKL, Madeo J, Sahoo C, et al., *Sci. Adv.* 2021;7:eabg0192.

ACKNOWLEDGMENTS

This work was funded by the Max Planck Society, the European Research Council (ERC) under the European Union's Horizon 2020 research and innovation and the H2020-EU.1.2.1. FET Open programs (Grant Numbers: ERC-2015-CoG-682843, ERC-2015-AdG-694097, and OPTologic 899794), the Max Planck Society's Research Network BiGmax on Big-Data-Driven Materials-Science, and the German Research Foundation (DFG) within the Emmy Noether program (Grant Number: RE 3977/1), through SFB 951 "Hybrid Inorganic/Organic Systems for Opto-Electronics (HIOS)" (Project Number: 182087777, projects B12 and B17), the SFB/TRR 227 "Ultrafast Spin Dynamics" (projects A09 and B07), the Research Unit FOR 1700 "Atomic Wires" (project E5), and the Priority Program SPP 2244 (project 443366970). Dominik Christiansen thanks the graduate school Advanced Materials (SFB 951) for support. Samuel Beaulieu acknowledges financial support from the NSERC-Banting Postdoctoral Fellowships Program. Tommaso Pincelli acknowledges financial support from the Alexander von Humboldt Foundation. Corrections added on October 7, 2022 after first online publication: Ethic Statement was missing.

AUTHOR CONTRIBUTIONS

Shuo Dong: Data curation (Lead); Formal analysis (Equal); Investigation (Lead); Methodology (Equal); Validation (Equal); Writing – original draft (Lead); Writing – review and editing (Equal). **Michele Puppin:** Data curation (Equal); Formal analysis (Equal); Investigation (Equal); Methodology (Equal); Writing – review and editing (Equal). **Tommaso Pincelli:** Data curation (Equal); Formal analysis (Equal); Investigation (Equal); Methodology (Equal); Software (Equal); Writing – review and editing (Equal). **Samuel Beaulieu:** Formal analysis (Equal); Investigation (Equal); Writing – review and editing (Equal). **Dominik Christiansen:** Investigation (Equal); Methodology (Equal); Software (Lead); Writing – review and editing (Equal). **Hannes Hübener:** Formal analysis (Equal); Investigation (Equal); Writing – review and editing (Equal). **Christopher Nicholson:** Investigation (Supporting); Methodology (Equal); Writing – review and editing (Equal). **Rui Patrick Xian:** Formal analysis (Equal); Software (Lead); Writing – review and editing (Equal). **Maciej Dendzik:** Investigation (Equal); Writing – review and editing (Equal). **Yunpei Deng:** Methodology (Equal). **Yoav William Windsor:** Methodology (Equal). **Malte Selig:** Investigation (Equal); Methodology (Equal); Writing – review and editing (Equal). **Ermin Malic:** Methodology (Supporting). **Angel Rubio:** Funding acquisition (Equal); Methodology (Equal); Resources (Equal); Supervision (Equal); Writing – review and editing (Equal). **Andreas Knorr:** Conceptualization (Equal); Funding acquisition (Equal); Methodology (Equal); Project administration (Equal); Resources (Equal); Supervision (Lead); Validation (Equal); Writing – review and editing (Equal). **Martin Wolf:** Conceptualization (Equal); Funding acquisition (Equal); Methodology (Equal); Resources (Equal);

Supervision (Equal); Writing–review & editing (Equal). **Laurenz Rettig**: Conceptualization (Lead); Data curation (Equal); Funding acquisition (Equal); Investigation (Equal); Methodology (Equal); Project administration (Equal); Resources (Equal); Supervision (Lead); Validation (Equal); Writing–review & editing (Equal). **Ralph Ernstorfer**: Conceptualization (Lead); Formal analysis (Equal); Funding acquisition (Lead); Methodology (Equal); Project administration (Lead); Resources (Lead); Supervision (Lead); Validation (Equal); Writing–review & editing (Equal).

CONFLICT OF INTEREST

The authors declare no conflict of interest.

ETHICS STATEMENT

The authors confirm that they have followed the ethical policies of the journal.

DATA AVAILABILITY STATEMENT

We provide the full experimental dataset as well as the details of the data analysis on the data repository Zenodo (<https://doi.org/10.5281/zenodo.4739195>). Also, we provide the source code of our data analytics on GitHub (<https://github.com/mpes-kit>).

TRANSPARENT PEER REVIEW

The peer review history for this article is available at <https://publons.com/publon/10.1002/ntls.10010>.

ORCID

Shuo Dong  <https://orcid.org/0000-0002-7940-9583>
 Michele Puppini  <https://orcid.org/0000-0002-1328-7165>
 Tommaso Pincelli  <https://orcid.org/0000-0003-2692-2540>
 Samuel Beaulieu  <https://orcid.org/0000-0003-2316-2224>
 Hannes Hübener  <https://orcid.org/0000-0003-0105-1427>
 Christopher W. Nicholson  <https://orcid.org/0000-0002-2885-4433>
 Rui Patrick Xian  <https://orcid.org/0000-0001-9895-6956>
 Maciej Dendzik  <https://orcid.org/0000-0002-4179-0040>
 Yoav William Windsor  <https://orcid.org/0000-0001-6371-5837>
 Angel Rubio  <https://orcid.org/0000-0003-2060-3151>
 Laurenz Rettig  <https://orcid.org/0000-0002-0725-6696>
 Ralph Ernstorfer  <https://orcid.org/0000-0001-6665-3520>

REFERENCES

- Frenkel J. On the transformation of light into heat in solids. I. *Phys Rev.* 1931;37:17.
- Perfetto E, Sangalli D, Marini A, Stefanucci G. First-principles approach to excitons in time-resolved and angle-resolved photoemission spectra. *Phys Rev B.* 2016;94:245303.
- Christiansen D, Selig M, Malic E, Ernstorfer R, Knorr A. Theory of exciton dynamics in time-resolved ARPES: intra- and intervalley scattering in two dimensional semiconductors. *Phys Rev B.* 2019;100:205401.
- Wang K, Kristiaan De G, Jauregui LA, et al. Electrical control of charged carriers and excitons in atomically thin materials. *Nat Nanotechnol.* 2018;13:128-132.
- Kaviraj B, Sahoo D. Physics of excitons and their transport in two dimensional transition metal dichalcogenide semiconductors. *RSC Adv.* 2019;9:25439-25461.
- Palumbo M, Bernardi M, Grossman JC. Exciton radiative lifetimes in two-dimensional transition metal dichalcogenides. *Nano Lett.* 2015;15:2794-2800.
- Yuan L, Wang T, Zhu T, Zhou M, Huang L. Exciton dynamics, transport, and annihilation in atomically thin two-dimensional semiconductors. *J Phys Chem Lett.* 2017;8:3371-3379.
- Christiansen D, Selig M, Berghäuser G, et al. Phonon sidebands in monolayer transition metal dichalcogenides. *Phys Rev Lett.* 2017;119:187402.
- Steinhoff A, Florian M, Rosner M, Schönhoff G, Wehling T, Jahnke F. Exciton fission in monolayer transition metal dichalcogenide semiconductors. *Nat Commun.* 2017;8:1166.
- Wang G, Chernikov A, Glazov MM, et al. Colloquium: excitons in atomically thin transition metal dichalcogenides. *Rev Mod Phys.* 2018;90:021001.
- Wang G, Marie X, Gerber I, et al. Giant enhancement of the optical second harmonic emission of WSe₂ monolayers by laser excitation at exciton resonances. *Phys. Rev. Lett.* 2015;114:097403.
- Li Y, Chernikov A, Zhang X, et al. Measurement of the optical dielectric function of monolayer transition-metal dichalcogenides: MoS₂, MoSe₂, WS₂, and WSe₂. *Phys Rev B.* 2014;90:205422.
- Pöllmann C, Steinleitner P, Leierseder U, et al. Resonant internal quantum transitions and femtosecond radiative decay of excitons in monolayer WSe₂. *Nat Mater.* 2015;14:889-893.
- Selig M, Berghäuser G, Raja A, et al. Excitonic linewidth and coherence lifetime in monolayer transition metal dichalcogenides. *Nat Commun.* 2016;7:13279.
- Zeng H, Dai J, Yao W, Xiao D, Cui X. Valley polarization in MoS₂ monolayers by optical pumping. *Nat. Nanotechnol.* 2012;7:490-493.
- Mak KF, He K, Shan J, Heinz TF. Control of valley polarization in monolayer MoS₂ by optical helicity. *Nat. Nanotechnol.* 2012;7:494-498.
- Bertoni R, Nicholson CW, Waldecker L, et al. Generation and evolution of spin-, valley-, and layer-polarized excited carriers in inversion-symmetric WSe₂. *Phys Rev Lett.* 2016;117:277201.
- Park S, Mütz N, Schultz T, et al. Direct determination of monolayer MoS₂ and WSe₂ exciton binding energies on insulating and metallic substrates. *2D Mater.* 2018;5:025003.
- Yao K, Yan A, Kahn S, et al. Optically discriminating carrier-induced quasiparticle band gap and exciton energy renormalization in monolayer MoS₂. *Phys Rev Lett.* 2017;119:087401.
- Klein J, Kerelsky A, Lorke M, et al. Impact of substrate induced band tail states on the electronic and optical properties of MoS₂. *Appl Phys Lett.* 2019;115:261603.
- Chernikov A, Berkelbach TC, Hill HM, et al. Exciton binding energy and nonhydrogenic Rydberg series in monolayer WS₂. *Phys Rev Lett.* 2014;113:076802.
- Puppini M, Deng Y, Nicholson CW, et al. Time- and angle-resolved photoemission spectroscopy of solids in the extreme ultraviolet at 500 kHz repetition rate. *Rev Sci Instrum.* 2019;90:023104.
- Weinelt M, Kutschera M, Fauster T, Rohlfing M. Dynamics of exciton formation at the Si (100) c (4 × 2) surface. *Phys Rev Lett.* 2004;92:126801.
- Madeo J, Man MKL, Sahoo C, et al. Directly visualizing the momentum forbidden dark excitons and their dynamics in atomically thin semiconductors. *Science.* 2020;370:1199-1204.
- Maklar J, Dong S, Beaulieu S, et al. A quantitative comparison of time-of-flight momentum microscopes and hemispherical analyzers for time-resolved ARPES experiments. *Rev Sci Instrum.* 2020;90:023105.
- Wickramaratne D, Zahid F, Lake RK. Electronic and thermoelectric properties of few-layer transition metal dichalcogenides. *J Chem Phys.* 2014;140:124710.

27. Rustagi A, Kemper AF. Photoemission signature of excitons. *Phys Rev B*. 2018;97:235310.
28. Perfetto E, Stefanucci G. Ultrafast creation and melting of nonequilibrium excitonic condensates in bulk WSe_2 . *arXiv*. Preprint posted online November 24, 2020. arXiv:2011.11967.
29. Knoesel E, Hotzel A, Wolf M. Ultrafast dynamics of hot electrons and holes in copper: excitation, energy relaxation, and transport effects. *Phys Rev B*. 1998;57:12812.
30. Hiromu U, Branko G. Theory of two-photon photoemission spectroscopy of surfaces. *Prog Surf Sci*. 2007;82:193-223.
31. Raja A, Selig M, Berghauser G, et al. Enhancement of exciton-phonon scattering from monolayer to bilayer WS_2 . *Nano Lett*. 2018;18:6135-6143.
32. Marini A. Ab initio finite-temperature excitons. *Phys Rev Lett*. 2008;101:106405.
33. Offenbacher H, Daniel L, Thomas U, et al. Orbital tomography: molecular band maps, momentum maps and the imaging of real space orbitals of adsorbed molecules *Electron. Spectrosc Relat Phenom*. 2015;204:92-101.
34. Puschnig P, Berkebile S, Fleming AJ, et al. Reconstruction of molecular orbital densities from photoemission data. *Science*. 2009;326:702-706.
35. Jansen M, Keunecke M, Duvel M, et al. Efficient orbital imaging based on ultrafast momentum microscopy and sparsity-driven phase retrieval. *New J Phys*. 2020;22:063012.
36. Wießner M, Hauschild D, Sauer C, Feyer V, Scholl A, Reinert F. Complete determination of molecular orbitals by measurement of phase symmetry and electron density. *Nat Commun*. 2014;5:41-56.
37. Beaulieu S, Schusser J, Dong S, et al. Revealing hidden orbital pseudospin texture with time-reversal dichroism in photoelectron angular distributions. *Phys Rev Lett*. 2020;125:216404.
38. Schüler M, Pincelli T, Dong S, et al. Bloch wavefunction reconstruction using multidimensional photoemission spectroscopy. *arXiv*. Preprint posted online March 31, 2021. arXiv:2021;2103.17168.

SUPPORTING INFORMATION

Additional supporting information may be found online in the Supporting Information section at the end of the article.

How to cite this article: Dong S, Puppim M, Pincelli T, et al. Direct measurement of key exciton properties: energy, dynamics and spatial distribution of the wave function. *Nat Sci*. 2021;1:e10010. <https://doi.org/10.1002/ntls.10010>